

Resolution limits of active triangulation systems by defocusing

Günther Seitz, MEMBER SPIE
H.-J. Tiziani, FELLOW SPIE
Universität Stuttgart
Institut für Technische Optik
7000 Stuttgart 80
Federal Republic of Germany

Abstract. In active triangulation systems, one side of the triangulation triangle is made up of a spatial light structure of well-known shape and location, causing a pattern on the surface of the target object. The other side of the triangle is embodied by ray bundles, imaging this pattern onto a position sensor. Because nearly all surfaces show scattering characteristics between specular and diffuse reflection, the corresponding image-forming wavefronts are not of uniform amplitude, and so the irradiance of the imaging pupil is also nonuniform. If the imaging is done by an aberrated system, this can cause deviations from the image as predicted by geometric optics. An estimate of deviations resulting from defocusing by treating the imaging process in terms of scalar diffraction theory, using a linear model for nonuniform pupil irradiance is given.

Subject terms: triangulation; defocused imaging; scalar diffraction theory.

Optical Engineering 32(6), 1374-1383 (June 1993).

1 Introduction

Triangulation systems are used in geodetical, astronomical, and industrial applications. In geodesy and astronomy, passive systems are of main importance. Because object distances are much larger than the aperture of the detection system, the entrance pupil is hit by a small patch of the radiance field proceeding from the target point. This patch covers a small solid angle and is therefore of virtually constant intensity. So, because the amplitude over the entrance pupil is uniform, we have to consider only the phase of the image-forming wavefront. The radial symmetry in the pupil is preserved and symmetrical phase aberrations, such as defocusing, affect only the image sharpness, not the affinity relation between object and image.

To avoid the correspondence problem, industrial applications are dominated by active triangulation systems. In active triangulation systems, one side of the triangle is made up of a spatial light structure, for example, a narrow light beam, causing a spot on the object surface. Because the reflectance map of most real-world surfaces is given as a superposition of several scattering lobes,¹ the shape of the corresponding radiance distribution usually shows a strong angular dependence. Because object distances are of the same order as the system aperture, the entrance pupil of the detection system covers a noninfinitesimal solid angle of this angular radiance distribution (see Fig. 3 in Sec. 3). We therefore have to take into consideration phase and amplitude of the image-forming wavefront. The shape of the accepted radiance patch depends highly on the distance, position, and surface slope of the spotted object point and therefore does not show any symmetry in respect to the optical axis of the detection system. Hence, we deal with a nonuniform radiance distribution with nonaxial symmetry. This leads to deviations

from the geometric image even for symmetrical aberrations, such as defocusing, because the radial symmetry in the pupil is disturbed.

As recommended by Häusler and Heckel² and Bickel et al.,³ triangulation systems with a spot- or line-related acquisition of range data can be arranged such that the influence of defocusing is reduced by fulfilling the Scheimpflug condition. The drawback of such Scheimpflug systems is, however, that scanning of the imaging ray bundles is necessary to acquire 2.5-dimensional surface maps. Telecentric systems⁴ allow Scheimpflug arrangement but are restricted in measurement volume to the aperture of the optical arrangement. Fringe projection systems, acquiring spatially resolved range maps from one⁵ or several video images,⁶ need neither scanning nor high-aperture optics but have to allow for a certain amount of defocusing.

Such non-Scheimpflug triangulation systems are attractive because they are less expensive. To estimate performance limits of such systems, a quantitative investigation of non-focused imaging at nonuniform pupil irradiance is necessary. This paper gives a worst-case estimation of measurement errors for non-Scheimpflug triangulation systems due to non-uniform pupil irradiance.

2 Experimental Observation of Position Errors

Figure 1 shows a simple arrangement to visualize position errors caused by nonuniform pupil irradiance. The beams of two He-Ne lasers are focused on a spark-eroded metallic surface with a roughness of $R_a = 0.4 \mu\text{m}$. The corresponding spots P_1 and P_2 are imaged onto a linear CCD array, using a lens with a focal length of $f = 25 \text{ mm}$ and a $f/\#$ of 2. Because we use a 4- f arrangement, the magnification is unity. Although both spots hit the same surface point, the resulting scattering lobes are proceeding in different directions because of the different incidence angles of the laser beams. Therefore, both spots are imaged at different levels of irradiance nonuniformity in the entrance pupil of the imaging system.

Paper 16111 received Nov. 21, 1991; revised manuscript received Oct. 5, 1992; accepted for publication Oct. 6, 1992.
© 1993 Society of Photo-Optical Instrumentation Engineers. 0091-3286/93/\$2.00.

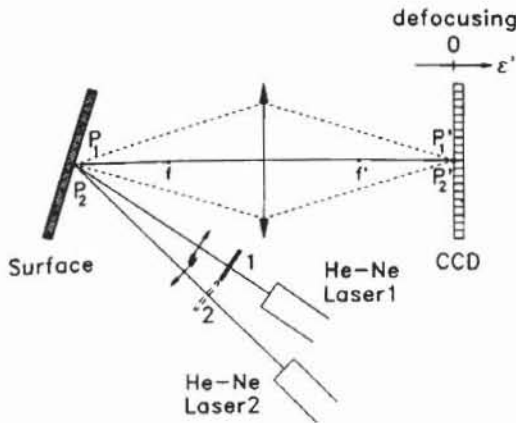


Fig. 1 Experimental setup for observation of position errors.

For both levels of nonuniformity, we take the positions of the corresponding image points P'_1 and P'_2 at several positions around the geometric optical focal plane. To compensate unintentional movements of the sensor normal to the optical axis, we use the position difference of P'_2 and P'_1 . The centroids of the images are taken as the point positions.

Centroid fluctuations of a Gaussian-shaped image point resulting from speckles can be estimated by⁷

$$\langle x_c^2 \rangle = \frac{1}{8\pi} \left(\frac{\lambda^2}{\Omega} \right) \quad (1)$$

where $\langle x_c^2 \rangle$ is the variance of the centroid position and Ω is the solid angle subtended by the pupil as seen from the image plane. Inserting λ and $\Omega = (2f\#)^{-2}$ we get, for the standard deviation of the centroid,

$$\sigma_c = \left(\frac{2}{\pi} \right)^{1/2} \lambda \approx 0.5 \mu\text{m} \quad (2)$$

The standard deviation of the position difference is roughly twice this value.

Figure 2 shows the position difference in dependence of defocusing. Because the corresponding object points are fixed and speckle noise cannot cause effects of that magnitude as shown, we have to conclude, that non-uniform irradiance of the entrance pupil is the reason for the increase of the position difference with increasing defocusing.

3 Nonfocused Imaging

Triangulation systems obtain distance information by measuring the angles of a plane triangle. Figure 3 shows an active triangulation arrangement with one side of the triangle PES made up of a narrow light ray, designating surface point P . A certain amount of the scattered radiance gets into the entrance pupil of the imaging system. The corresponding image point P' defines only one point of the ray representing the other side of the triangle.

Because at least two points are necessary for fixing a ray, knowledge of a second ray point is required. For a uniform irradiance of the entrance pupil and aberration-free optics, this second point is given by the center of the entrance pupil E , and therefore the image lies spatially along the principal ray. For a nonuniform radiance distribution, this cannot be maintained.

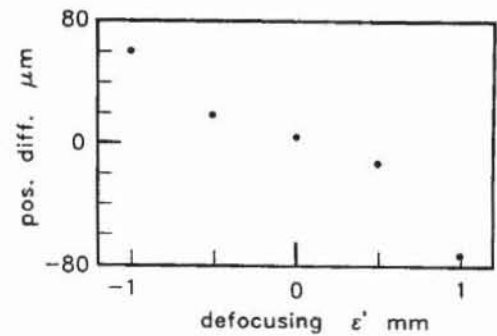


Fig. 2 Position difference versus defocusing.

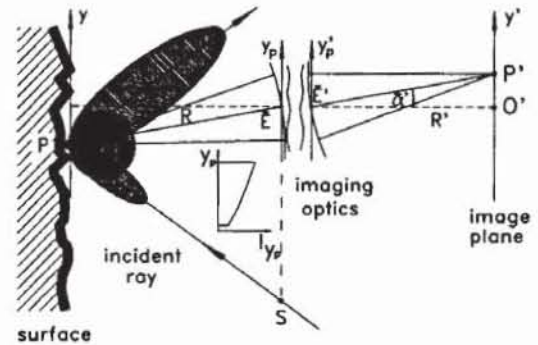


Fig. 3 Active triangulation system.

To investigate the spatial behavior of the image point P' for nonuniform radiance distribution, we take a look at the imaging process. Assuming a Fresnel number $Z = r^2/(\lambda f)$ far beyond unity, the imaging process can be treated in terms of Fresnel diffraction.⁸

Assuming a linear passive system, the image U'_i of an object U_o results from the convolution integral

$$U'_i(x', y') = \iint_{-\infty}^{\infty} h(x' - x, y' - y) U_o(x, y) dx dy \quad (3)$$

If the isoplanatic condition is given, the amplitude point spread function (PSF) $h(x' - x, y' - y)$ can be written⁹

$$h(x' - \hat{x}, y' - \hat{y}) = \frac{1}{A} \iint_{-\infty}^{\infty} P(x'_p, y'_p) \exp[ikW(x_p'^2 + y_p'^2)] \times \exp\left\{ -ik\frac{1}{R'} [(x' - \hat{x})x'_p + (y' - \hat{y})y'_p] \right\} dx'_p dy'_p \quad (4)$$

with magnified object coordinates

$$\hat{x} = \beta' x, \quad \hat{y} = \beta' y,$$

and defocusing

$$W = \frac{1}{2} \left(\frac{1}{R'} + \frac{1}{R} - \frac{1}{f'} \right) \quad (5)$$

where β' is the lateral magnification, f' is the focal length,

and R and R' are the radii of the entering wavefront respective to the leaving wavefront (see Fig. 3).

The pupil function $P(x'_p, y'_p)$ represents the amplitude of the imaging wavefront. Using Hopkins' canonical coordinates,¹⁰

$$X'_s = \frac{x'_p}{r'_s}, \quad Y'_t = \frac{y'_p}{N' r'_t}, \quad (6)$$

$$u'_s = (n \sin \alpha'_s) \frac{x'_p}{\lambda}, \quad v'_t = n(\sin \alpha'_t - \sin \bar{\alpha}') \frac{y'_p}{\lambda},$$

where N' is the direction cosine of the effective pupil ray; $\bar{\alpha}'$, α'_s , and α'_t are the angles of sagittal and tangential marginal rays; and r'_s and r'_t are the corresponding aperture radii. Hopkins's coordinates rely on the normalization of the pupil coordinates to their maximum value and the coordinates of object and image plane to their respective numerical aperture. This results in image and pupil coordinates independent from aperture size and magnification.

Restricting to points near the optical axis, we can assume equal-sized tangential and sagittal pupils:

$$r'_s = r'_t = r'_t. \quad (7)$$

Then, the final amplitude PSF is given by the integral over the area A' of the normalized pupil:

$$h(u'_s, v'_t) = \frac{1}{A'} \iint_{A'} P(X'_s, Y'_t) \exp[ikW_{20}(X'^2_s + Y'^2_t)] \times \exp[-i2\pi(X'_s u'_s + Y'_t v'_t)] dX'_s dY'_t, \quad (8)$$

where the quantity A is the amplitude at the geometrical image ($u'_s = v'_t = 0$) for uniform pupil irradiance and zero defocusing [see appendix Eq. (26)]. Defocusing W_{20} is given by

$$W_{20} = \frac{r'^2}{2} \left(\frac{1}{R'} + \frac{1}{R} - \frac{1}{f'} \right). \quad (9)$$

For small amounts of defocusing, the relation between defocusing W_{20} and focus distance ϵ' can be obtained by linearizing W_{20} about the focal plane:

$$W_{20} \approx -\frac{1}{2} \left(\frac{r'}{R'} \right)^2 \epsilon'. \quad (10)$$

4 Imaging with Nonuniform Pupil Irradiance

We describe the nonuniform radiance distribution in the entrance pupil by the pupil function

$$P(X_s, Y_t) = 1 + \omega Y_t. \quad (11)$$

Assuming aberration-free optics, this pupil function propagates to the exit pupil with a magnification of unity.

Within the scope of this linear model, we can select any value between the limiting cases of uniform ($\omega = 0$) and nonuniform ($\omega = 1$) radiance amplitude over the entrance pupil.

Inserting this pupil function into Eq. (8), we obtain, for the amplitude PSF:

$$h(u'_s, v'_t) = \frac{1}{A'} \iint_{A'} (1 + \omega Y'_t) \exp[ikW_{20}(X'^2_s + Y'^2_t)]$$

$$\times \exp[-i2\pi(X'_s u'_s + Y'_t v'_t)] dX'_s dY'_t. \quad (12)$$

Optical triangulation arrangements obtain the distance information from the one-dimensional point position within the epipolar plane. Consequently, we restrict our considerations to the epipolar section of the PSF. Assuming worst-case conditions, we choose the gradient of nonuniformity in the epipolar plane. The analytical calculation of the PSF according to Eq. (12) is given in the appendix.

Using the substitutions

$$\begin{aligned} \bar{W}_{20} &= 2kW_{20}, \\ \bar{u}'_s &= 2\pi u'_s, \\ \bar{v}'_t &= 2\pi v'_t, \end{aligned} \quad (13)$$

we obtain the amplitude/intensity PSF within the geometric shadow boundary ($|\bar{v}'_t/\bar{W}_{20}| < 1$) from Eqs. (58) and (59):

$$h(\bar{v}'_t, \bar{W}_{20}) = \frac{2}{\bar{W}_{20}} \left(\bar{\omega} \left\{ i \exp\left(-i \frac{\bar{v}'^2_t}{2\bar{W}_{20}}\right) - \exp\left(i \frac{\bar{W}_{20}}{2}\right) \right. \right. \\ \left. \left. \times [iV_0(\bar{v}'_t, \bar{W}_{20}) + V_1(\bar{v}'_t, \bar{W}_{20})] \right\} \right. \\ \left. - \omega J_1(\bar{v}'_t) \exp\left(i \frac{\bar{W}_{20}}{2}\right) \right), \quad (14)$$

$$|h(\bar{v}'_t, \bar{W}_{20})|^2 = \left(\frac{2}{\bar{W}_{20}} \right)^2 \{ [\bar{\omega} \bar{V}_0(\bar{v}'_t, \bar{W}_{20})]^2 \\ + [\bar{\omega} \bar{V}_1(\bar{v}'_t, \bar{W}_{20}) + \omega J_1(\bar{v}'_t)]^2 \}, \quad (15)$$

respectively, from Eqs. (46) and (47) in the geometric shadow ($|\bar{v}'_t/\bar{W}_{20}| > 1$):

$$h(\bar{v}'_t, \bar{W}_{20}) = \frac{2}{\bar{W}_{20}} \exp\left(i \frac{\bar{W}_{20}}{2}\right) \left\{ U_1(\bar{v}'_t, \bar{W}_{20}) - iU_2(\bar{v}'_t, \bar{W}_{20}) \right. \\ \left. - \omega \frac{\bar{v}'_t}{\bar{W}_{20}} [iU_2(\bar{v}'_t, \bar{W}_{20}) + U_3(\bar{v}'_t, \bar{W}_{20})] \right\}, \quad (16)$$

$$|h(\bar{v}'_t, \bar{W}_{20})|^2 = \left(\frac{2}{\bar{W}_{20}} \right)^2 \left\{ \left[U_1(\bar{v}'_t, \bar{W}_{20}) - \omega \frac{\bar{v}'_t}{\bar{W}_{20}} U_3(\bar{v}'_t, \bar{W}_{20}) \right]^2 \right. \\ \left. + [\bar{\omega} U_2(\bar{v}'_t, \bar{W}_{20})]^2 \right\}, \quad (17)$$

with the substitutions

$$\begin{aligned} \bar{V}_0(\bar{v}'_t, \bar{W}_{20}) &= V_0(\bar{v}'_t, \bar{W}_{20}) - \cos\left(\frac{\bar{W}_{20}}{2} + \frac{\bar{v}'^2_t}{2\bar{W}_{20}}\right), \\ \bar{V}_1(\bar{v}'_t, \bar{W}_{20}) &= V_1(\bar{v}'_t, \bar{W}_{20}) - \sin\left(\frac{\bar{W}_{20}}{2} + \frac{\bar{v}'^2_t}{2\bar{W}_{20}}\right), \\ \bar{\omega} &= \omega \frac{\bar{v}'_t}{\bar{W}_{20}} + 1. \end{aligned} \quad (18)$$

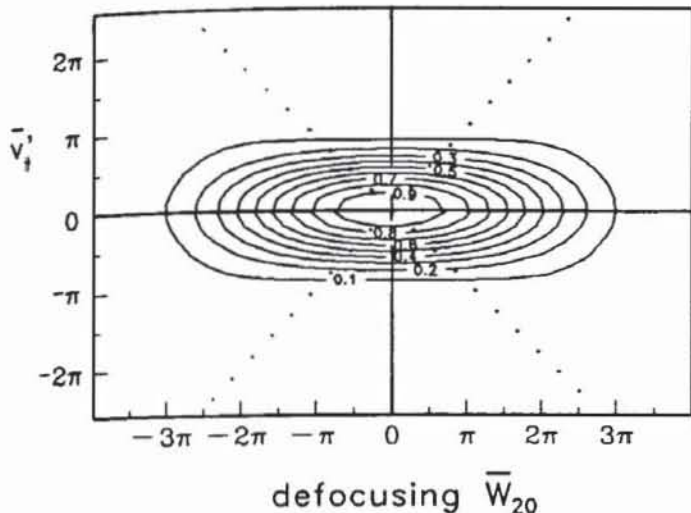


Fig. 4 Isophotes near focus in the epipolar plane for uniform pupil irradiance ($\omega=0$); dotted lines: boundary of geometric shadow.

The quantities V_i and U_i denote Lommel functions.¹¹ The conditions $|\bar{v}'_i/\bar{W}_{20}| > 1$ and $|\bar{v}'_i/\bar{W}_{20}| < 1$ divide image space with respect to the geometric optical shadow boundary, given by

$$y' = \pm \frac{r'}{R'} |\epsilon'|, \quad (19)$$

for an axial image point in real-world coordinates.

The intensity PSF gives the intensity distribution of a δ -shaped object point in image space. Figures 4 and 5 show the corresponding intensity distributions for the limiting cases of uniform and nonuniform pupil irradiance ($\omega=0$ respective $\omega=1$). For uniform pupil irradiance, Fig. 4 shows the intensity distribution symmetrical to the principal ray, which remains symmetrical even outside the geometric focal plane. According to Fig. 5, this is not the case for nonuniform pupil irradiance. In this case, the intensity distribution is tilted with respect to the principal ray $\bar{v}'_i = 0$.

Figures 6 and 7 show sections through the isophotes plots given in Figs. 4 and 5 for defocusing $\bar{W}_{20} = 0$ and $\bar{W}_{20} = \pi$. In case of uniform pupil irradiance, the intensity distribution remains symmetrical with respect to the geometric image position $\bar{v}'_i = 0$. For nonuniform pupil irradiance, this symmetry is only given in the focal plane $\bar{W}_{20} = 0$. Apart from the focal plane, the intensity distribution loses its symmetry and is displaced from the geometric image $\bar{v}'_i = 0$.

From the appendix, Eq. (61), we obtain the dependence of the position of the intensity maximum \bar{v}'_{im} on defocusing \bar{W}_{20} and nonuniformity ω :

$$\bar{v}'_{im}(\bar{W}_{20}, \omega) = \left\{ \begin{array}{l} \frac{8 \left[\sin\left(\frac{\bar{W}_{20}}{4}\right) \right]^2 - \bar{W}_{20} \omega \sin\left(\frac{\bar{W}_{20}}{2}\right)}{2\bar{W}_{20} \left[\sin\left(\frac{\bar{W}_{20}}{4}\right) \right]^2 \left[4\left(\frac{\omega}{\bar{W}_{20}}\right)^2 - 1 \right]} \\ -2\omega^2 \sin\left(\frac{\bar{W}_{20}}{2}\right) + \bar{W}_{20}(\omega^2/2) \end{array} \right\} \quad (20)$$

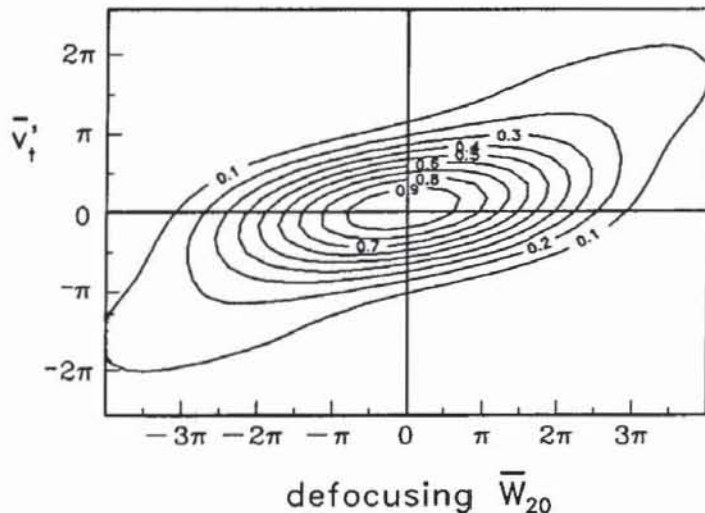


Fig. 5 Isophotes near focus in the epipolar plane for nonuniform pupil irradiance ($\omega=1$).

Figure 8 shows the behavior of the intensity maximum with respect to defocusing according to Eq. (20) for nonuniform pupil irradiance $\omega=1$. It can be seen that the position of the maximum intensity \bar{v}'_{im} depends approximately linearly on defocusing \bar{W}_{20} . The dependence of the maximum intensity on the nonuniformity ω is given in Fig. 9 for defocusing $\bar{W}_{20} = \pi$. A nearly linear dependence also exists.

Figure 10 illustrates these results for a simple imaging arrangement. According to Fig. 10(a), the maximum intensity coincides with the principal ray for uniform pupil irradiance. Consequently, we obtain the principal ray at any image plane within the depth of focus. According to Fig. 10(b), this is not the case for nonuniform pupil irradiance. Even within the depth of focus, consistence between the maximum intensity and the principal ray is not given. Maximum intensity and principal ray coincide only in the focal plane. So, an image point P'_d captured outside the focal plane results in a virtual object point P''_d .

5 Estimation of Position Errors

To get a worst-case estimate of position errors caused by nonuniform pupil irradiance, we select our image plane at the border of depth of focus and assume the largest possible nonuniformity. According to Born and Wolf,¹¹ the depth of focus in optical imaging is given by $\Delta\bar{W}_{20} \approx \pm 3.2$. Using defocusing $\bar{W}_{20} = \pi$ and assuming a nonuniformity of $\omega = +1$, we investigate the position error of different sized Gaussian and harmonic objects given by

$$G(\bar{v}'_i) = \exp\left[-\left(\frac{\bar{v}'_i}{b}\right)^2\right], \quad (21)$$

respective

$$S(\bar{v}'_i) = \cos\left(2\pi \frac{\bar{v}'_i}{b}\right). \quad (22)$$

The calculations are done for coherent and incoherent imaging by convolving the objects with the corresponding PSF. Figure 11 shows the position errors of the Gaussian and the harmonic object in dependence of the (normalized) size parameter b . It can be seen that for incoherent imaging, the

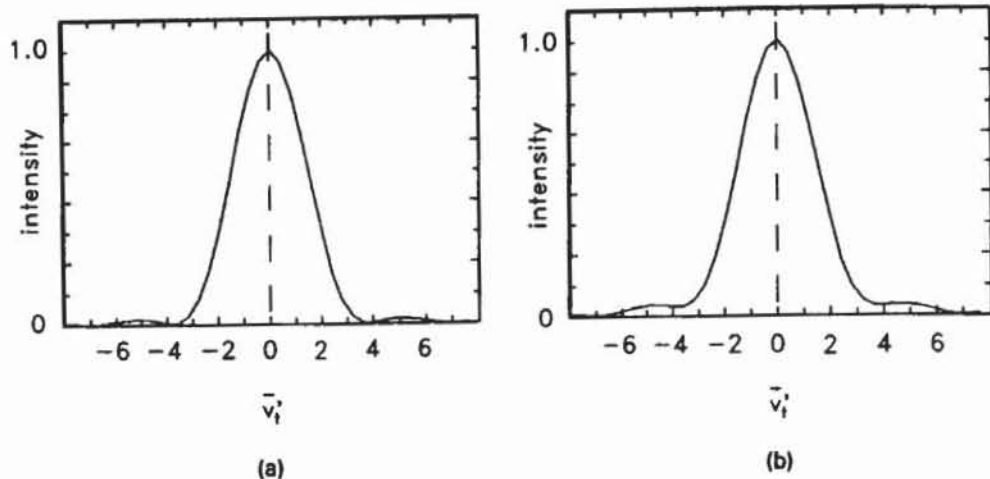


Fig. 6 Sections through the intensity distribution (Figs. 4 and 5) for uniform pupil irradiance ($\omega = 0$); (a) Gaussian focus $\overline{W}_{20} = 0$ and (b) depth of focus boundary $\overline{W}_{20} = \pi$.

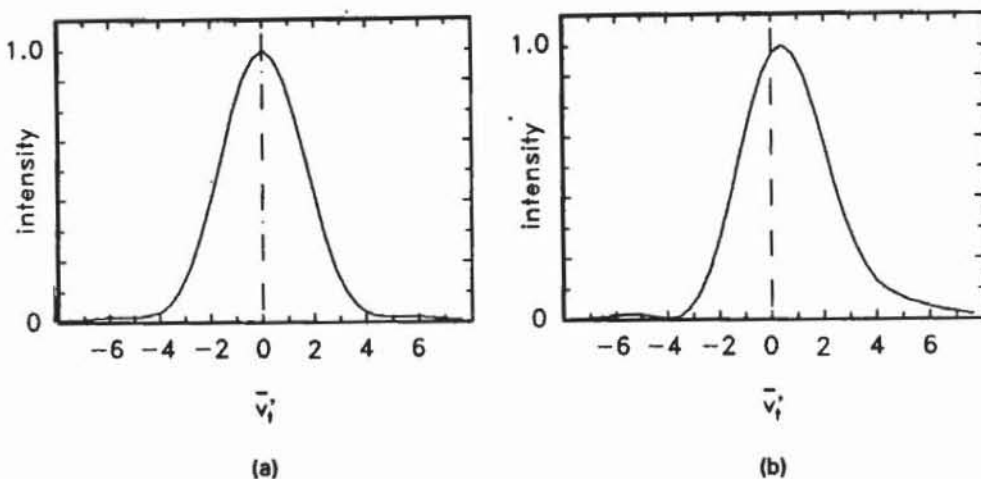


Fig. 7 Sections through the intensity distribution for nonuniform pupil irradiance ($\omega = 1$); (a) Gaussian focus $\overline{W}_{20} = 0$ and (b) depth of focus boundary $\overline{W}_{20} = \pi$.

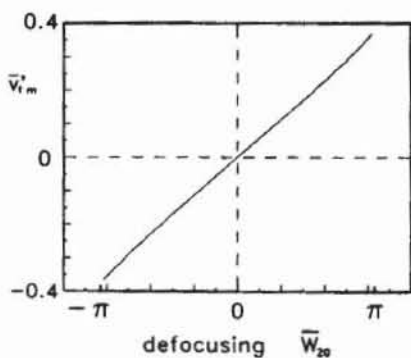


Fig. 8 Maximum of the intensity PSF as a function of defocusing for nonuniform pupil irradiance ($\omega = 1$).

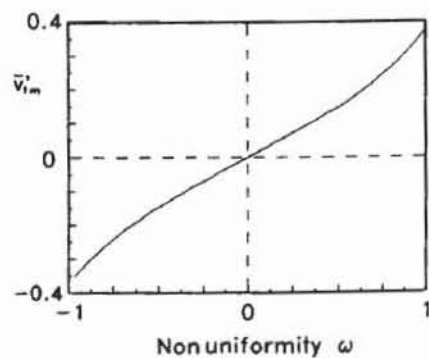


Fig. 9 Maximum of the intensity PSF as a function of the irradiance nonuniformity for defocusing $\overline{W}_{20} = \pi$.

position error depends only slightly on the size of the objects and is of the same order of magnitude for both object types. For coherent imaging, the position error is much smaller and depends more on type and size of the imaged objects.

To get the position errors in real-world coordinates, we can transform back from normalized coordinates by using the Eqs. (6), (7), and (13). Assuming a refractive index of unity, we can write for points near the optical axis:

$$y' = \frac{\overline{v}_i' \lambda}{2\pi \sin(\alpha_i')} \quad (23)$$

Normalizing this coordinate to the diameter of the diameter of the Airy disc,

$$y'_a = 2 \cdot 1.22 \frac{\lambda}{2 \sin(\alpha_i')} \quad (24)$$

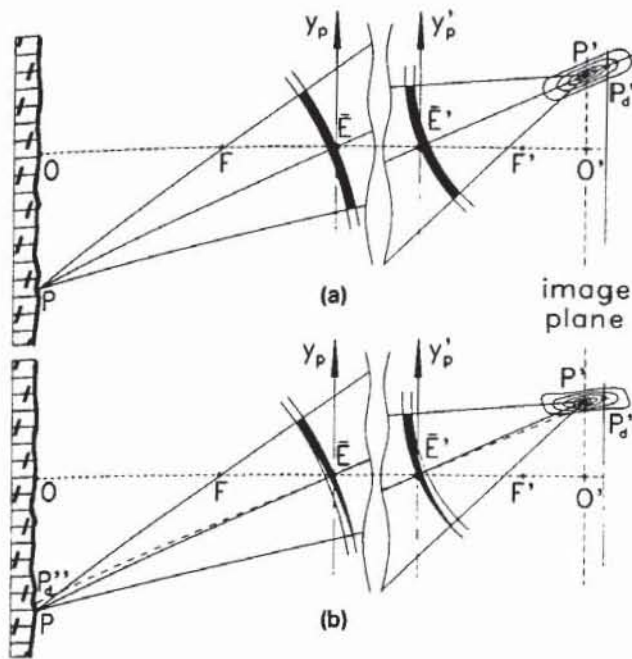


Fig. 10 Imaging ray bundles for (a) uniform and (b) nonuniform pupil irradiance (isophotes represented enlarged).

we obtain image space coordinates in terms of the diffraction limited image point:

$$y'_A = \frac{\bar{v}'_i}{4\pi 1.22} \quad (25)$$

Taking 0.7 as mean value for the incoherent position errors from Fig. 11, we get a normalized value of 0.046 from Eq. (25). If we remember that the nonuniformity ω can also be -1 , this means that the position error is $\pm 4.5\%$ the size of the unperturbed image point.

Note that these calculations are only valid for diffraction-limited optics. For aberrated optics, a larger position error must be expected.

Reducing the numerical aperture and thus increasing depth of focus also increases the absolute displacement \bar{v}'_i at the limit of depth of focus. But reducing the aperture results also in a smaller patch of the scattering lobe being accepted by the entrance pupil of the imaging optics. Consequently, if we assume a smooth radiance distribution, the radiance difference between the edges of the aperture decreases and so the inhomogeneity is reduced.

6 Ray Evaluation with Nonuniform Pupil Irradiance

According to Fig. 8, the position of the intensity maximum depends approximately linearly on defocusing. So, the maximum intensity lies along a ray, which we call the propagation ray. Because this ray crosses the geometric image point, it is a valid geometric construction ray. Consequently, tracing this ray through the optical system leads to the object point P , yielding the unknown side of triangulation triangle. In contrast to the principal ray, the propagation ray does not pass through the pupil centers \bar{E}' and \bar{E} .

Therefore, we need a second point for fixing this ray. Figure 12 shows a suitable arrangement: the propagation ray

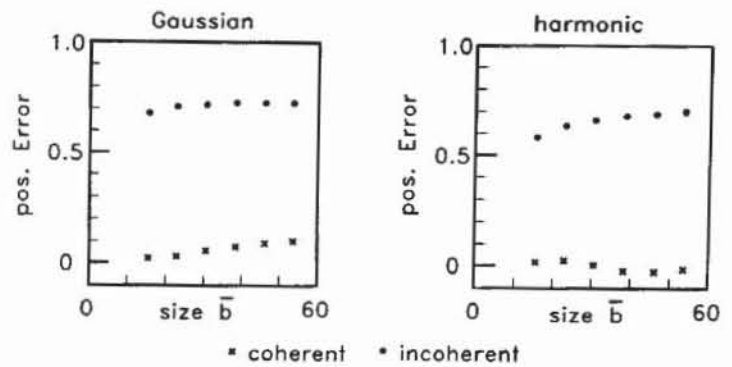


Fig. 11 Calculated position errors for Gaussian and harmonic objects versus object size.

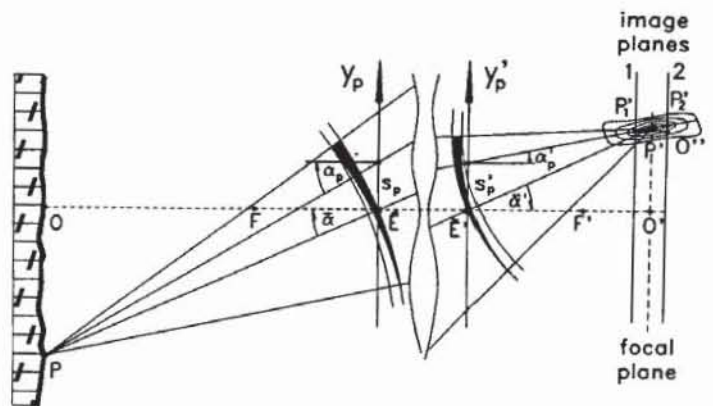


Fig. 12 Ray evaluation by ray tracing.

is captured in two image planes within the depth of focus. From both images we obtain the angle α'_p and height s'_p of the propagation ray. Because the observed section of the propagation ray is restricted to depth of focus, the measurement triangle $P'_1P'_2O''$ for evaluating α'_p is usually small compared to the triangle $\bar{E}'P'O'$ for measuring angle $\bar{\alpha}'$ of the principal ray. The propagation ray detection therefore requires higher position resolution for obtaining comparable measurement accuracy. Because the resolution requirement is reduced for a larger triangle, the propagation ray detection becomes more suitable with increasing depth of focus.

7 Conclusions

We have given a quantitative estimation of measurement errors caused by a nonuniform irradiated imaging pupil for nonfocused imaging. Even within the depth of focus, these errors can reach up to $\pm 4.5\%$ of the size of the unperturbed image point for incoherent imaging. For coherent imaging, the position errors are smaller and more sensitive to the shape of the imaged object.

It has been shown that the position error depends nearly linearly on defocusing for a linear radiance distribution in the imaging pupil. Within the scope of this linear model, the maximum of intensity defines a ray in the image space. For small numerical apertures, this ray can be used to obtain the missing side of the triangulation triangle by optical ray tracing, thus overcoming errors caused by defocusing and non-uniform radiance distribution.

8 Appendix: Calculation of PSF for Nonuniform Pupil Irradiance

Using the substitutions

$$X' = X'_s, \quad Y' = Y'_t,$$

$$u' = \bar{u}'_s, \quad v' = \bar{v}'_t,$$

$$\bar{W} = \bar{W}_{20},$$

the PSF is given by

$$h(u', v', \bar{W}, \omega) = \frac{1}{A} \iint_{A'} (1 + \omega X') \exp \left[i \frac{\bar{W}}{2} (X'^2 + Y'^2) \right] \times \exp[-i(X'u' + Y'v')] dX' dY', \quad (26)$$

with

$$A = \iint_{A'} \exp[i(X'u' + Y'v')] dX' dY' = \pi,$$

for circular aperture and $u' = v' = 0$. The PSF is normalized to the value of a diffraction-limited system in geometric focus for uniform amplitude distribution over the entrance pupil.

Using Hopkins's canonical pupil coordinates, the integration extends over the unit circle. So we transform to cylindrical coordinates:

$$X' = r' \sin(\varphi'), \quad Y' = r' \cos(\varphi'),$$

$$u' = \rho' \sin(\psi'), \quad v' = \rho' \cos(\psi'), \quad (27)$$

$$h(\rho', \psi', \bar{W}, \omega) = \frac{1}{\pi} \int_0^{2\pi} \int_0^1 [1 + \omega r' \cos(\varphi')] \exp \left\{ -i\rho' r' \times [\cos(\varphi') \cos(\psi') + \sin(\varphi') \sin(\psi')] + i \frac{\bar{W}}{2} r'^2 \right\} r' dr' d\varphi'. \quad (28)$$

We calculate the PSF in the tangential plane $\psi' = 0$ and $\psi' = \pi$, the direction of the nonuniformity gradient. So the sine terms vanish and we can back substitute the plane coordinate $v' = \rho' \cos(\psi')$:

$$h(v', \bar{W}, \omega) = \frac{1}{\pi} \int_0^{2\pi} \int_0^1 [1 + \omega r' \cos(\varphi')] \times \exp \left[-iv' r' \cos(\varphi') + i \frac{\bar{W}}{2} r'^2 \right] r' dr' d\varphi'. \quad (29)$$

The PSF is split into two expressions, corresponding to a constant and a linear part:

$$h(v', \bar{W}, \omega) = \frac{1}{\pi} [h_1(v', \bar{W}) + \omega h_2(v', \bar{W})], \quad (30)$$

with

$$h_1(v', \bar{W}) = \int_0^{2\pi} \int_0^1 \exp \left[-iv' r' \cos(\varphi') + i \frac{\bar{W}}{2} r'^2 \right] r' dr' d\varphi', \quad (31)$$

and

$$h_2(v', \bar{W}) = \int_0^{2\pi} \int_0^1 \exp \left\{ i[\varphi' - v' r' \cos(\varphi')] + i \frac{\bar{W}}{2} r'^2 \right\} \times r'^2 dr' d\varphi', \quad (32)$$

using the relation

$$\int_0^{2\pi} \sin(\phi) \exp[i\tau \cos(\phi)] d\phi = 0.$$

With the Bessel function

$$J_k(\tau) = \frac{i^{-k}}{2\pi} \int_0^{2\pi} \exp\{i[k\phi + \tau \cos(\phi)]\} d\phi,$$

and substitutions

$$\eta = v' r' \quad \kappa = i\bar{W} \left(\frac{1}{v'} \right)^2, \quad (33)$$

we obtain, for h_1 and h_2 , respectively,

$$h_n(v', \bar{W}) = -2\pi \left(-i \frac{1}{v'} \right)^{n+1} \int_0^{v'} \eta^n J_{n-1}(\eta) \times \exp \left(\frac{\kappa}{2} \eta^2 \right) d\eta. \quad (34)$$

Using the relation

$$\frac{d}{d\eta} [\eta^n J_n(\eta)] = \eta^n J_{n-1}(\eta), \quad (35)$$

we can write

$$h_n(v', \bar{W}) = -2\pi \left(-i \frac{1}{v'} \right)^{n+1} \int_0^{v'} \frac{d}{d\eta} [\eta^n J_n(\eta)] \times \exp \left(\frac{\kappa}{2} \eta^2 \right) d\eta, \quad (36)$$

or

$$h_n(v', \bar{W}) = -2\pi \left(-\frac{i}{v'}\right)^{n+1} \frac{1}{\kappa} \int_0^{v'} \eta^{n-1} J_{n-1}(\eta) \frac{d}{d\eta} \times \left[\exp\left(\frac{\kappa}{2}\eta^2\right) \right] d\eta \quad (37)$$

Integration by parts of Eq. (36) leads to

$$\int \frac{d}{d\eta} [\eta^n J_n(\eta)] \exp\left(\frac{\kappa}{2}\eta^2\right) d\eta = \left[\eta^n J_n(\eta) \exp\left(\frac{\kappa}{2}\eta^2\right) \right] - \kappa \int \eta^{n+1} J_n(\eta) \exp\left(\frac{\kappa}{2}\eta^2\right) d\eta \quad (38)$$

By successively repeating this step, we obtain

$$\int \frac{d}{d\eta} \left[\eta^n J_n(\eta) \right] \exp\left(\frac{\kappa}{2}\eta^2\right) d\eta = \left\{ \exp\left(\frac{\kappa}{2}\eta^2\right) \kappa^{-n} [(\eta\kappa)^n J_n(\eta) - (\kappa\eta)^{n+1} J_{n+1}(\eta) + (\kappa\eta)^{n+2} J_{n+2}(\eta) - (\kappa\eta)^{n+3} J_{n+3}(\eta) + (\kappa\eta)^{n+4} J_{n+4}(\eta) - \dots + \dots] \right\} \quad (39)$$

In the same way from (37), we obtain

$$\int \eta^{n-1} J_{n-1}(\eta) \frac{d}{d\eta} \left[\exp\left(\frac{\kappa}{2}\eta^2\right) \right] d\eta = \exp\left(\frac{\kappa}{2}\eta^2\right) \kappa^{-n} [(\kappa\eta)^{n-1} J_{n-1}(\eta) - (\kappa\eta)^{n-2} J_{n-2}(\eta) + (\kappa\eta)^{n-3} J_{n-3}(\eta) - (\kappa\eta)^{n-4} J_{n-4}(\eta) + \dots - \dots] \quad (40)$$

By back substitution of Eq. (33) and using integration limits $r'=0, 1$, from Eq. (39), we obtain

$$h_1(v', \bar{W}) = 2\pi \frac{1}{\bar{W}} \exp\left(i\frac{\bar{W}}{2}\right) \left[\left(\frac{\bar{W}}{v'}\right) J_1(v') - i\left(\frac{\bar{W}}{v'}\right)^2 J_2(v') - \left(\frac{\bar{W}}{v'}\right)^3 J_3(v') + \dots - \right] \quad (41)$$

$$h_2(v', \bar{W}) = -2\pi \frac{v'}{\bar{W}^2} \exp\left(i\frac{\bar{W}}{2}\right) \left[i\left(\frac{\bar{W}}{v'}\right)^2 J_2(v') + \left(\frac{\bar{W}}{v'}\right)^3 J_3(v') - i\left(\frac{\bar{W}}{v'}\right)^4 J_4(v') - \dots + \right] \quad (42)$$

The sums of Bessel functions can be expressed by Lommel functions. Lommel functions $U_n(v', \bar{W})$ and $V_n(v', \bar{W})$ show a different convergence behavior with respect to v'/\bar{W} :

$$U_n(v', \bar{W}) = \sum_{s=0}^{\infty} (-1)^s \left(\frac{\bar{W}}{v'}\right)^{n+2s} J_{n+2s}(v') \quad \text{if } |v'/\bar{W}| > 1, \quad (43a)$$

$$V_n(v', \bar{W}) = \sum_{s=0}^{\infty} (-1)^s \left(\frac{v'}{\bar{W}}\right)^{n+2s} J_{n+2s}(v') \quad \text{if } |v'/\bar{W}| < 1. \quad (43b)$$

For $|v'/\bar{W}| > 1$, the sum of products in Eqs. (41) and (42) can be expressed by Lommel functions $U_n(v', \bar{W})$:

$$h_1(v', \bar{W}) = 2\pi \frac{1}{\bar{W}} \exp\left(i\frac{\bar{W}}{2}\right) [U_1(v', \bar{W}) - iU_2(v', \bar{W})] \quad (44)$$

$$h_2(v', \bar{W}) = -2\pi \frac{v'}{\bar{W}^2} \exp\left(i\frac{\bar{W}}{2}\right) [iU_2(v', \bar{W}) + U_3(v', \bar{W})] \quad (45)$$

Outside the geometric optical shadow ($|v'/\bar{W}| > 1$), we obtain for the amplitude PSF after back substituting $\bar{W} = \bar{W}_{20}$ and $v = \bar{v}'_r$,

$$h(\bar{v}'_r, \bar{W}_{20}, \omega) = \frac{2}{\bar{W}_{20}} \exp\left(i\frac{\bar{W}_{20}}{2}\right) \left\{ U_1(\bar{v}'_r, \bar{W}_{20}) - iU_2(\bar{v}'_r, \bar{W}_{20}) - \omega \frac{\bar{v}'_r}{\bar{W}_{20}} [iU_2(\bar{v}'_r, \bar{W}_{20}) + U_3(\bar{v}'_r, \bar{W}_{20})] \right\} \quad (46)$$

The intensity PSF results from the squared modulus of the amplitude PSF:

$$|h(\bar{v}'_r, \bar{W}_{20}, \omega)|^2 = \left(\frac{2}{\bar{W}_{20}}\right)^2 \left\{ \left[U_1(\bar{v}'_r, \bar{W}_{20}) - \omega \frac{\bar{v}'_r}{\bar{W}_{20}} U_3(\bar{v}'_r, \bar{W}_{20}) \right]^2 + \left(\omega \frac{\bar{v}'_r}{\bar{W}_{20}} + 1 \right)^2 [U_2(\bar{v}'_r, \bar{W}_{20})]^2 \right\} \quad (47)$$

Similarly, the intensity distribution inside geometrical shadow boundary ($|v'/\bar{W}| < 1$) results from Eq. (40) by back substituting Eq. (33):

$$\int_0^{v'} \eta^1 J_0(\eta) \exp\left(\frac{\kappa}{2}\eta^2\right) d\eta = -i \left(\frac{\bar{W}}{v'}\right)^{-1} \left\{ \exp\left(i\frac{\bar{W}}{2} r'^2\right) \times \left[J_0(v' r') + i\left(\frac{\bar{W} r'}{v'}\right)^{-1} J_{-1}(v' r') - \left(\frac{\bar{W} r'}{v'}\right)^{-2} J_{-2}(v' r') - i\left(\frac{\bar{W} r'}{v'}\right)^{-3} J_{-3}(v' r') + \left(\frac{\bar{W} r'}{v'}\right)^{-4} J_{-4}(v' r') + \dots - \dots \right] \right\}_{r'=0}^1 \quad (48)$$

Using the relations

$$J_{-n}(x) = (-1)^n J_n(x) \quad \lim_{x \rightarrow 0} \frac{J_n(x)}{x^n} = \frac{1}{2^n n!} \quad (49)$$

we obtain

$$\int_0^{v'} \eta^1 J_0(\eta) \exp\left(\frac{\kappa}{2}\eta^2\right) d\eta = \left(\frac{\tilde{W}}{v'^2}\right)^{-1} \left\{ \exp\left(i\frac{\tilde{W}}{2}\right) \left[-iJ_0(v') \right. \right. \\ \left. \left. - \left(\frac{\tilde{W}}{v'}\right)^{-1} J_1(v') + i\left(\frac{\tilde{W}}{v'}\right)^{-2} J_2(v') + \left(\frac{\tilde{W}}{v'}\right)^{-3} J_3(v') \right. \right. \\ \left. \left. - i\left(\frac{\tilde{W}}{v'}\right)^{-4} J_4(v') - \dots + \dots \right] + i \left[1 - i\frac{1}{2}\left(\frac{\tilde{W}}{v'^2}\right)^{-1} \right. \right. \\ \left. \left. - \frac{1}{8}\left(\frac{\tilde{W}}{v'^2}\right)^{-2} + i\frac{1}{48}\left(\frac{\tilde{W}}{v'^2}\right)^{-3} + \frac{1}{384}\left(\frac{\tilde{W}}{v'^2}\right)^{-4} - \dots \right] \right\}. \quad (50)$$

Inside the geometric shadow boundary $|v'/\tilde{W}| < 1$, we can express the sums of products by Lommel functions $V_n(v', \tilde{W})$:

$$h_1(v', \tilde{W}) = 2\pi \frac{1}{\tilde{W}} \left\{ \exp\left(i\frac{\tilde{W}}{2}\right) [-iV_0(v', \tilde{W}) - V_1(v', \tilde{W})] \right. \\ \left. + i \exp\left(-i\frac{v'^2}{2\tilde{W}}\right) \right\}. \quad (51)$$

And similarly for $h_2(v', \tilde{W})$,

$$\int_0^{v'} \eta^2 J_1(\eta) \exp\left(\frac{\kappa}{2}\eta^2\right) d\eta = -\left(\frac{\tilde{W}}{v'^2}\right)^{-2} \left\{ \exp\left(i\frac{\tilde{W}}{2}\right) \left[\right. \right. \\ \left. \left. \times \left[i\left(\frac{\tilde{W}r'}{v'}\right) J_1(v'r') - J_0(v'r') - i\left(\frac{\tilde{W}r'}{v'}\right)^{-1} J_{-1}(v'r') \right. \right. \right. \\ \left. \left. + \left(\frac{\tilde{W}r'}{v'}\right)^{-2} J_{-2}(v'r') + i\left(\frac{\tilde{W}r'}{v'}\right)^{-3} J_{-3}(v'r') \right. \right. \\ \left. \left. - \left(\frac{\tilde{W}r'}{v'}\right)^{-4} J_{-4}(v'r') - \dots + \dots \right] \right\}_{r'=0}, \quad (52)$$

$$\int_0^{v'} \eta^2 J_1(\eta) \exp\left(\frac{\kappa}{2}\eta^2\right) d\eta = \left(\frac{\tilde{W}}{v'^2}\right)^{-2} \left\{ \exp\left(i\frac{\tilde{W}}{2}\right) \left[\right. \right. \\ \left. \left. \times \left[V_0(v', \tilde{W}) - i\left(\frac{\tilde{W}}{v'}\right) J_1(v') - iV_1(v', \tilde{W}) \right] \right. \right. \\ \left. \left. - \left[\cos\left(\frac{v'^2}{2\tilde{W}}\right) - i \sin\left(\frac{v'^2}{2\tilde{W}}\right) \right] \right\}. \quad (53)$$

Then, $h_2(v', \tilde{W})$ is given by

$$h_2(v', \tilde{W}) = -2\pi \frac{v'}{\tilde{W}^2} \left\{ \exp\left(i\frac{\tilde{W}}{2}\right) \left[iV_0(v', \tilde{W}) + \left(\frac{\tilde{W}}{v'}\right) J_1(v') \right. \right. \\ \left. \left. + V_1(v', \tilde{W}) \right] - i \exp\left(-i\frac{v'^2}{2\tilde{W}}\right) \right\}. \quad (54)$$

Back substituting $\tilde{W} = \bar{W}_{20}$ and $v' = \bar{v}'_r$ and using the substitutions

$$\tilde{V}_0(\bar{v}'_r, \bar{W}_{20}) = V_0(\bar{v}'_r, \bar{W}_{20}) - \cos\left(\frac{\bar{W}_{20}}{2} + \frac{\bar{v}'_r{}^2}{2\bar{W}_{20}}\right), \quad (55)$$

$$\tilde{V}_1(\bar{v}'_r, \bar{W}_{20}) = V_1(\bar{v}'_r, \bar{W}_{20}) - \sin\left(\frac{\bar{W}_{20}}{2} + \frac{\bar{v}'_r{}^2}{2\bar{W}_{20}}\right), \quad (56)$$

$$\tilde{\omega} = \left(\omega \frac{\bar{v}'_r}{\bar{W}_{20}} + 1 \right), \quad (57)$$

we obtain the amplitude/intensity PSF within the geometric shadow boundary:

$$h(\bar{v}'_r, \bar{W}_{20}, \omega) = \frac{2}{\bar{W}_{20}} \left(\tilde{\omega} \left\{ i \exp\left(-i\frac{\bar{v}'_r{}^2}{2\bar{W}_{20}}\right) - \exp\left(i\frac{\bar{W}_{20}}{2}\right) \right. \right. \\ \left. \left. \times [iV_0(\bar{v}'_r, \bar{W}_{20}) + V_1(\bar{v}'_r, \bar{W}_{20})] \right\} \right. \\ \left. - \omega J_1(\bar{v}'_r) \exp\left(i\frac{\bar{W}_{20}}{2}\right) \right) \quad (58)$$

$$|h(\bar{v}'_r, \bar{W}_{20}, \omega)|^2 = \left(\frac{2}{\bar{W}_{20}}\right)^2 \{ [\tilde{\omega} \tilde{V}_0(\bar{v}'_r, \bar{W}_{20})]^2 \\ + [\tilde{\omega} \tilde{V}_1(\bar{v}'_r, \bar{W}_{20}) + \omega J_1(\bar{v}'_r)]^2 \}. \quad (59)$$

Within the geometric shadow ($|v'/\bar{W}_{20}| > 1$), the intensity distribution is given by Eq. (47).

Using the relations

$$\frac{d}{dv'} \tilde{V}_0 = -J_1(v') - \frac{v'}{\bar{W}_{20}} \tilde{V}_1,$$

$$\frac{d}{dv'} \tilde{V}_1 = \frac{v'}{\bar{W}_{20}} \tilde{V}_0,$$

we obtain the derivation of Eq. (59) with respect to \bar{v}'_r

$$\frac{d}{d\mu} |h(\bar{v}'_r, \bar{W}_{20}, \omega)|^2 = 2 \left(\frac{2}{\bar{W}_{20}}\right)^2 \left[\tilde{\omega} \left(\frac{\omega}{\bar{W}_{20}} \{ [\tilde{V}_0(\bar{v}'_r, \bar{W}_{20})]^2 \right. \right. \\ \left. \left. + [\tilde{V}_1(\bar{v}'_r, \bar{W}_{20})]^2 \} - \tilde{V}_0(\bar{v}'_r, \bar{W}_{20}) J_1(\bar{v}'_r) \right. \right. \\ \left. \left. + \omega \tilde{V}_1(\bar{v}'_r, \bar{W}_{20}) J_0(\bar{v}'_r) \right) + \omega J_1(\bar{v}'_r) \right. \\ \left. \times \left[\omega J_0(\bar{v}'_r) - \frac{\tilde{V}_1(\bar{v}'_r, \bar{W}_{20}) + \omega J_1(\bar{v}'_r)}{\bar{v}'_r} \right] \right] \quad (60)$$

Setting Eq. (59) to zero yields the condition for maximum intensity. If we restrict our calculation to linear terms in \bar{v}'_r , we obtain

$$\bar{v}'_{om}(\bar{W}_{20}, \omega) = \left(\begin{array}{l} 8 \left[\sin\left(\frac{\bar{W}_{20}}{4}\right) \right]^2 - \bar{W}_{20} \omega \sin\left(\frac{\bar{W}_{20}}{2}\right) \\ 2\bar{W}_{20} \left[\sin\left(\frac{\bar{W}_{20}}{4}\right) \right]^2 \left[4\left(\frac{\omega}{\bar{W}_{20}}\right)^2 - 1 \right] \\ - 2\omega^2 \sin\left(\frac{\bar{W}_{20}}{2}\right) + \bar{W}_{20}(\omega^2/2) \end{array} \right) \quad (61)$$

Acknowledgment

We acknowledge the financial support by the German Research Council in the SFB 158 project.

References

1. H. D. Tagare and R. J. P. deFigueiredo, "A theory of photometric stereo for a class of diffuse non-Lambertian surfaces," *IEEE Trans. Pattern Anal. Machine Intell.* PAMI-13(2), 133-152 (1991).
2. G. Häusler and W. Heckel, "Light sectioning with large depth and with high resolution," *Appl. Opt.* 27(24), 5165-5169 (1988).
3. G. Bickel, G. Häusler, and M. Maul, "Triangulation with expanded range of depth," *Opt. Eng.* 24(6), 978-980 (1985).
4. G. Häusler and M. Maul, "Telecentric scanner for 3-D sensing," *Opt. Eng.* 24(6), 978-980 (1985).
5. M. Takeda and S. Kobayashi, "Fourier-transform method of fringe-pattern analysis for computer-based topography and interferometry," *J. Opt. Soc. Am.* 72(1), 156-160 (1982).
6. K. Sato and S. Inokuchi, "Range-imaging system utilizing nematic liquid crystal mask," in *Proc. 1st Int. Conf. on Computer Vision* (1987).
7. R. B. Baribeau and M. Rioux, "Centroid fluctuations of speckled targets," *Appl. Opt.* 30(26), 3752-3755 (1991).
8. Y. Li and E. Wolf, "Three-dimensional intensity distribution near focus in systems of different Fresnel numbers," *J. Opt. Soc. Am.* 1(8), 801-808 (1984).
9. J. W. Goodman, *Introduction to Fourier Optics*, McGraw-Hill, New York (1968).
10. C. S. Chung and H. H. Hopkins, "Influence of non-uniform amplitude on PSF," *J. Mod. Opt.* 35(9), 1485-1511 (1988).
11. M. Born and E. Wolf, *Principles of Optics*, 6th ed., Pergamon Press (1980).
12. H. H. Hopkins and M. J. Yzuel, "The computation of diffraction patterns in the presence of aberrations," *Opt. Acta* 17(3), 157-182 (1970).



Günther Seitz received his PhD from the University of Stuttgart in 1990. His doctoral thesis concerned optical surface measurement techniques for industrial applications. At present, he is working on optical measurement techniques at Carl Zeiss, Oberkochen.



H.-J. Tiziani was trained as a technician in optics and precision mechanics at Wild Heerbrugg and studied mechanical engineering in St. Gallen and optics at the Institut d'Optique in Paris. After his PhD with Hopkins at the Imperial College, London, he directed a summer school at IBM in San Jose, and was a consultant to IBM. From 1968 to 1973 he built the optics group at the federal Institute of Technology in Zürich (ETH). From 1973 to 1978 he was head-director of the central laboratory at Wild Heerbrugg, and since 1978 he has been a director of the Institute of Applied Optics and professor at the University of Stuttgart. He was dean and deputy dean of the faculty of mechanical engineering of the University of Stuttgart and is now president of the Great Senat. In addition, he was president of European Electro Optics, president of the Optics Division of the European Physical Society, and governor of SPIE. He has written more than 100 papers in different fields of applied optics. His main interests are the study of the quality of optical images and systems and the influence of centering errors. He has worked on speckle and speckle application, the application of computer-generated holograms for testing aspherical surfaces, surface profile and shape analysis using interferometry, heterodyne techniques and image processing, optical correlations, and photo-refractive materials.